Journal of Materials Chemistry C

ROYAL SOCIETY OF CHEMISTRY

PAPER

View Article Online
View Journal | View Issue

Cite this: J. Mater. Chem. C, 2026, 14, 5790

V-shaped D–π–A–π–D molecules based on benzothiophene-*S*,*S*-dioxide: tuning of excited states *via* donor strength to engineer photoactive materials

Mattia Zangoli, †[ab] Antonio Maggiore, †[c] Nicol Spallacci,[a] Fabrizio Mariano,[c] Filippo Monti, *[a] Soraia Flammini,[a] Marco Pugliese, [c] Giuseppe Gigli,[d] Vincenzo Maiorano[c] and Francesca Di Maria *[ab]

Received 2nd December 2025,
Accepted 5th February 2026

DOI: 10.1039/d5tc04245c

rsc.li/materials-c

Controlling locally excited (LE) and charge-transfer (CT) states and triplet-related pathways is crucial for the design of photoactive materials. Here, it is reported a family of V-shaped D–π–A–π–D small molecules (**V-CBZ$_2$**, **V-POZ$_2$**, and **V-PTZ$_2$**) that share a benzothiophene-*S*,*S*-dioxide acceptor and 1,4-dimethylphenylene bridges, while incorporating donors of increasing strength: carbazole, phenoxazine, and phenothiazine. The enforced V-shaped geometry limits the electronic coupling between the acceptor and donor units and prevents tight π–π stacking. Photophysical characterizations and TD-DFT calculations reveal that the donor strength dictates the nature of the excited states: from hybrid LE-CT character in **V-CBZ$_2$** to predominantly CT in **V-POZ$_2$** and **V-PTZ$_2$**. In solution, **V-CBZ$_2$** behaves as a bright fluorophore that predominantly decays radiatively (PLQY up to 100%), whereas **V-POZ$_2$** and **V-PTZ$_2$** act as efficient singlet-oxygen ($^1O_2$) photosensitizers (Φ_Δ up to 89%). Increasing solvent polarity stabilizes their CT states, further modulating emission lifetimes, PLQYs and $^1O_2$ generation. All compounds exhibit a reversible electrochromic response between transparent and coloured states, demonstrating that systematic donor variation provides straightforward control over the colour hue. In the solid state, all molecules show broad and featureless emission, with comparable PLQYs in doped polymer matrices and neat films, indicating that the twisted architecture effectively mitigates aggregation-induced quenching. Time-resolved studies reveal purely prompt fluorescence for **V-CBZ$_2$**, whereas **V-POZ$_2$** and **V-PTZ$_2$** display additional microsecond delayed components attributed to thermally activated delayed fluorescence (TADF). Finally, a solution-processed OLED based on a neat **V-CBZ$_2$** layer delivers broad white electroluminescence, highlighting that this V-shaped D–π–A–π–D architecture can function as a versatile platform for matrix-free solution-processable organic light-emitting materials.

I. Introduction

The design of donor–acceptor–donor (D–A–D) molecular architectures has emerged as a powerful approach for developing next-generation organic emitters with tunable optoelectronic properties for use in different applications.[1,2] In particular, such systems have demonstrated considerable potential in organic light-emitting diodes (OLEDs), electrochromic devices, sensors, and other technologies relying on controlled excited-state dynamics and tailored emission response.[3–8]

A key design principle in D–A–D systems is the fine modulation of the spatial arrangement and electronic communication between the donor and acceptor moieties, which critically impacts photophysical behaviour, charge transport properties, and exciton dynamics.[9–12] In such architectures, photoexcitation typically induces intramolecular charge transfer (ICT) processes - characterized by a redistribution of the electron density from donor units toward acceptor fragments within the same molecule.[13–21] For controlling the ICT strength is essential to fine-tune the energy levels and transition dipole moments,

[a] CNR-ISOF – Istituto per la Sintesi Organica e la Fotoreattività, via P. Gobetti 101, 40129 Bologna, Italy. E-mail: filippo.monti@cnr.it, francescagiulia.dimaria@cnr.it
[b] CLAN – Center for Light Activated Nanostructures c/o ISOF-CNR, via P. Gobetti 101, 40129 Bologna, Italy
[c] CNR-NANOTEC – Institute of Nanotechnology, c/o Campus Ecotekne, Via Monteroni, Lecce, 73100, Italy
[d] Department of Mathematics and Physics, University of Salento, Via Monteroni, Lecce, 73100, Italy
† M. Z. and A. M. contributed equally to this work.

minimize non-radiative decay channels, and enhance radiative recombination, all of which are critical factors for achieving high-performance emission in optoelectronics.[13–21] These characteristics are largely governed by the nature of the D–A pairs and their coupling strength. Among the different molecular topologies explored, bent D–A–D structures, such as U, V-shaped, or folded geometries, have attracted increasing attention.[22–28] Compared to planar architectures,[29] these geometries promote spatial decoupling between A and D units, which allows to (i) minimize π-conjugation in the ground state, (ii) reduce the overlap between the HOMO (typically located on the donor) and the LUMO (on the acceptor), and (iii) restrict electronic delocalization. Furthermore, their bent molecular geometry disfavors intermolecular π–π stacking interactions in the solid state, thereby mitigating aggregation-induced quenching (AIQ), a key requirement in many high-performance OLED applications and thermally activated delayed fluorescence (TADF).[30–33] Within these bent motifs, rigid V-shaped architectures are especially appealing because their two arms adopt a divergent arrangement, offering a simple topological handle to control fragment orientation and coupling within a common D–A–D framework. Furthermore, compared to more folded U-shaped motifs that can facilitate closer cofacial interactions, this divergent geometry can often reduce the probability of extended face-to-face packing in the solid state, further reducing intermolecular π–π stacking and aggregation-driven quenching.[34–36]

In this regard, we synthesized and characterized a novel family of V-shaped D–π–A–π–D small molecules (namely, **V-CBZ$_2$**, **V-PTZ$_2$**, and **V-POZ$_2$**) having a common electron-accepting core and identical π-spacers but differing in their electron-donating units (Chart 1).

In particular, the central acceptor unit is an oxidized benzo[*b*]thiophene-*S*,*S*-dioxide, chosen for its strong electron-withdrawing character.[30] This core is symmetrically flanked by two 1,4-dimethyl phenylene spacers, which enforce a nearly orthogonal arrangement between D and A planes, resulting in a rigid, non-planar V-shaped molecular architecture. By varying the donor units – *i.e.*, carbazole (CBZ), phenoxazine (POZ), or phenothiazine (PTZ) – we systematically tune the electron-donating strength without altering significantly the overall geometry. In particular, CBZ is a well-established donor in organic electronics characterized by a planar and rigid structure with moderate electron-rich character, whereas POZ and PTZ, incorporating oxygen and sulfur heteroatoms, respectively, exhibit stronger donor strength and greater conformational flexibility (CBZ < POZ ≈ PTZ).[37] This allows a rational exploration of the influence of the donor strength on photophysical properties in an electronically decoupled architecture. Photophysical characterizations, in combination with DFT calculations, show that varying the donor strength significantly alters the excited-state energy landscape made of multiple local excited (LE) and charge-transfer (CT) character minima, thereby modulating emission wavelengths, excited-state lifetimes and quantum yields, singlet-oxygen ($^1O_2$) photosensitization efficiency (Φ_Δ), solvatochromic and electrochromic behaviour. Finally, we demonstrate that the V-shaped architecture suppresses supramolecular ordered structures in the solid state, as indicated by X-ray diffraction. Among the series, in **V-POZ$_2$** and **V-PTZ$_2$**, containing the most electron-rich moieties, the presence of a stabilized CT state leads to strong fluorescence quenching. Anyway, such CT stabilization leads to a reduction of the singlet–triplet energy gap (ΔE_{ST}), enabling thermally activated delayed fluorescence (TADF) *via* reverse intersystem crossing (rISC). By contrast, **V-CBZ$_2$** exhibits a hybrid LE-CT emissive state with a high PLQY in the solid state, both when dispersed in doped matrices and as a neat film. Interestingly, a neat **V-CBZ$_2$** layer integrated into a prototype OLED produced white electroluminescence, validating the design and highlighting its potential as a matrix-free, solution-processable emissive material.

II. Results and discussion

2.1. Synthesis of V-shaped molecules

Scheme 1 illustrates the synthetic strategy employed to prepare the V-shaped D–π–A–π–D molecules, namely, **V-CBZ$_2$**, **V-POZ$_2$**, and **V-PTZ$_2$**, consisting of three consecutive steps common to all target compounds.

In the first step, the D groups (*i.e.*, CBZ, POZ, PTZ) were covalently attached to the 1,4-dimethyl phenylene spacers by

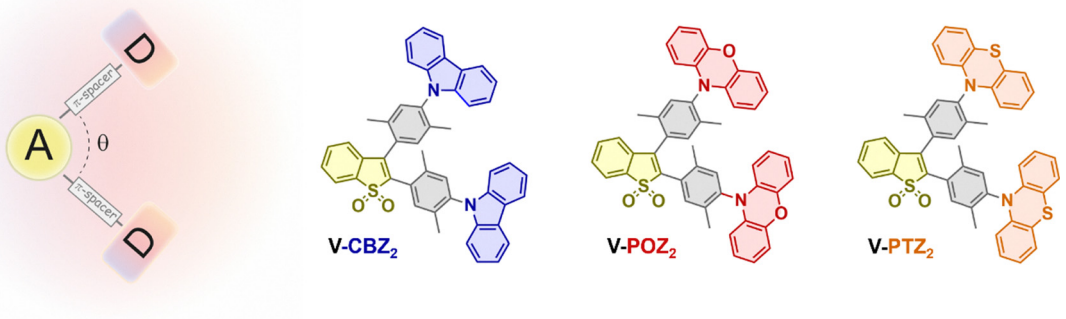

Chart 1 Molecular structures of V-shaped D–π–A–π–D molecules.

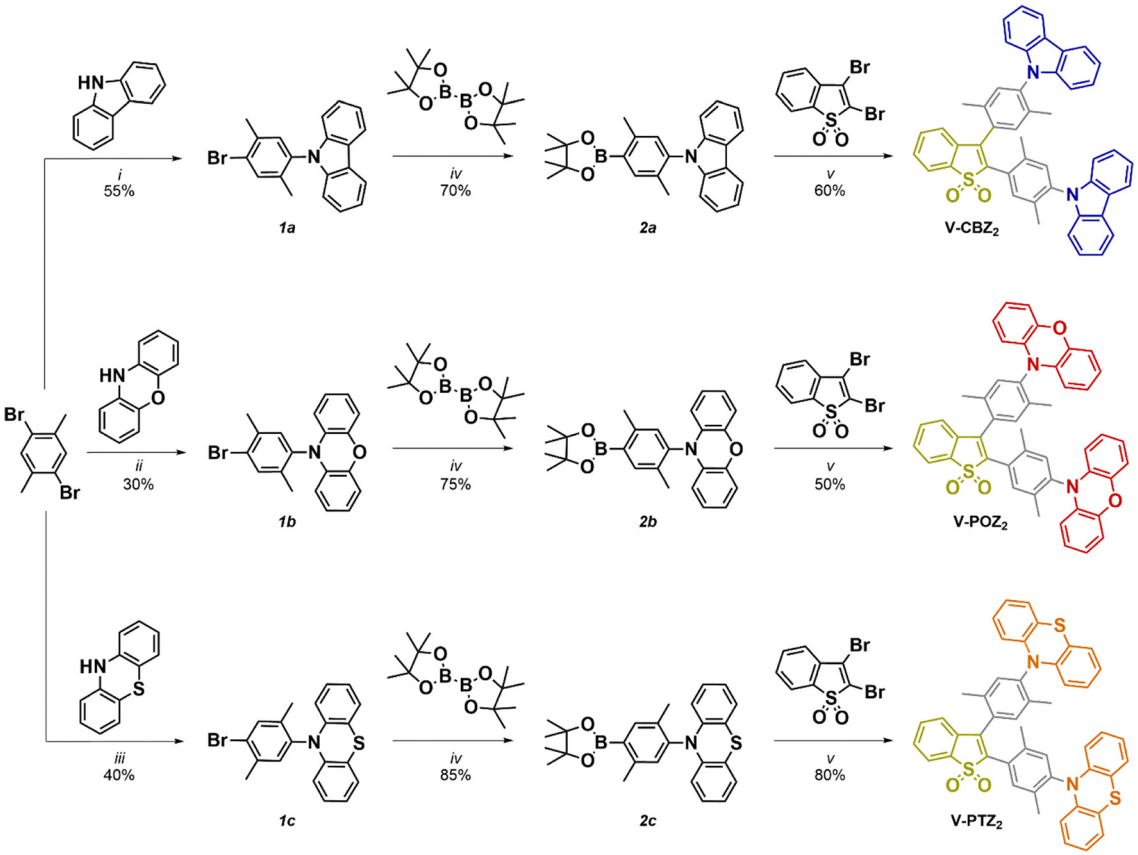

i. Carbazole (CBZ), $CuCO_4$, K_2CO_3, 200°C, overnight; ***ii.*** Phenoxazine (POZ), EtMgBr, $NiCl_2$(dppp), Toluene,110°C, overnight; ***iii.*** Phenothiazine (PTZ), *t*BuONa, $Pb(dba)_2$,$[(t\text{-}Bu)_3PH]BF_4$, Toluene, 110°C, overnight; ***iv.*** Bis(pinacolato)diboron, KOAc, $PdCl_2$(dppf), Dioxane, 100°C, overnight; ***v.*** 2,3-dibromobenzo[*b*]thiophene 1,1-dioxide, $NaHCO_3$, $PdCl_2$(dppf),THF/H_2O (2/1), 80°C, MW, 30 min.

Scheme 1 Synthesis of **V-CBZ$_2$**, **V-POZ$_2$**, and **V-PTZ$_2$** molecules.

forming an aromatic carbon-nitrogen bond. This coupling reaction was found to be highly sensitive to the nature of the D unit, requiring tailored synthetic protocols to access the brominated intermediates (**1a–c**, see Table S1). Specifically, the CBZ derivative (**1a**) was synthesized through an Ullmann-type N-arylation reaction, whereas the POZ and PTZ intermediates (**1b**, **1c**) were prepared *via* Buchwald–Hartwig amination reactions catalyzed by palladium and nickel, respectively.[38,39] In the second step, these intermediates were converted in high yield into boronate ester intermediates (**2a-c**) *via* Miyaura borylation.[40] Finally, the three V-shaped D–π–A–π–D molecules, which differ only in the D unit, were synthesized in good yields *via* microwave-assisted Suzuki cross-coupling reactions between the dibrominated *S*,*S*-dioxide-benzo[*b*]thiophene acceptor and the respective donor boronates.

Additional synthetic and characterization details are provided in the SI (Schemes S1–S4 and Fig. S1–S23). All molecules exhibit excellent solubility in common organic solvents at room temperature, favoured by their intrinsic twisted molecular geometry that hampers strong intermolecular interactions.

2.2. Photophysical characterization and DFT interpretation

2.2.1. Absorption properties. Fig. 1a–c show the UV-Vis absorption spectra of the **V-CBZ$_2$**, **V-POZ$_2$**, and **V-PTZ$_2$** molecules recorded in solvents of increasing polarity (*i.e.*, cyclohexane (CH), toluene (TOL), and dichloromethane (DCM)). All corresponding data are summarized in Table S2. For comparison, the spectra of the individual donors (*i.e.*, CBZ, POZ, and PTZ) and the acceptor fragment (based on the benzothiophene *S*,*S*-dioxide core linked to two phenylene spacers) are reported in Fig. S24.

As observed, the absorption profiles of all compounds: (i) closely resemble, both in shape and energy, those of their D–A individual component, suggesting a weak electronic coupling within the D–π–A–π–D framework, and (ii) remain largely unaffected by solvent polarity.

This behaviour can be rationalized considering the molecular geometries. DFT calculations reveal that, in the ground state, the optimized structures of all three compounds adopt a strongly bent, V-shaped geometry where: (i) the asymmetric benzothiophene *S*,*S*-dioxide acceptor links the two donors by forming a dihedral angle between the two units and the acceptor anchoring point at approximately 52° ± 4° for all molecules; (ii) the two methyl substituents on the phenylene

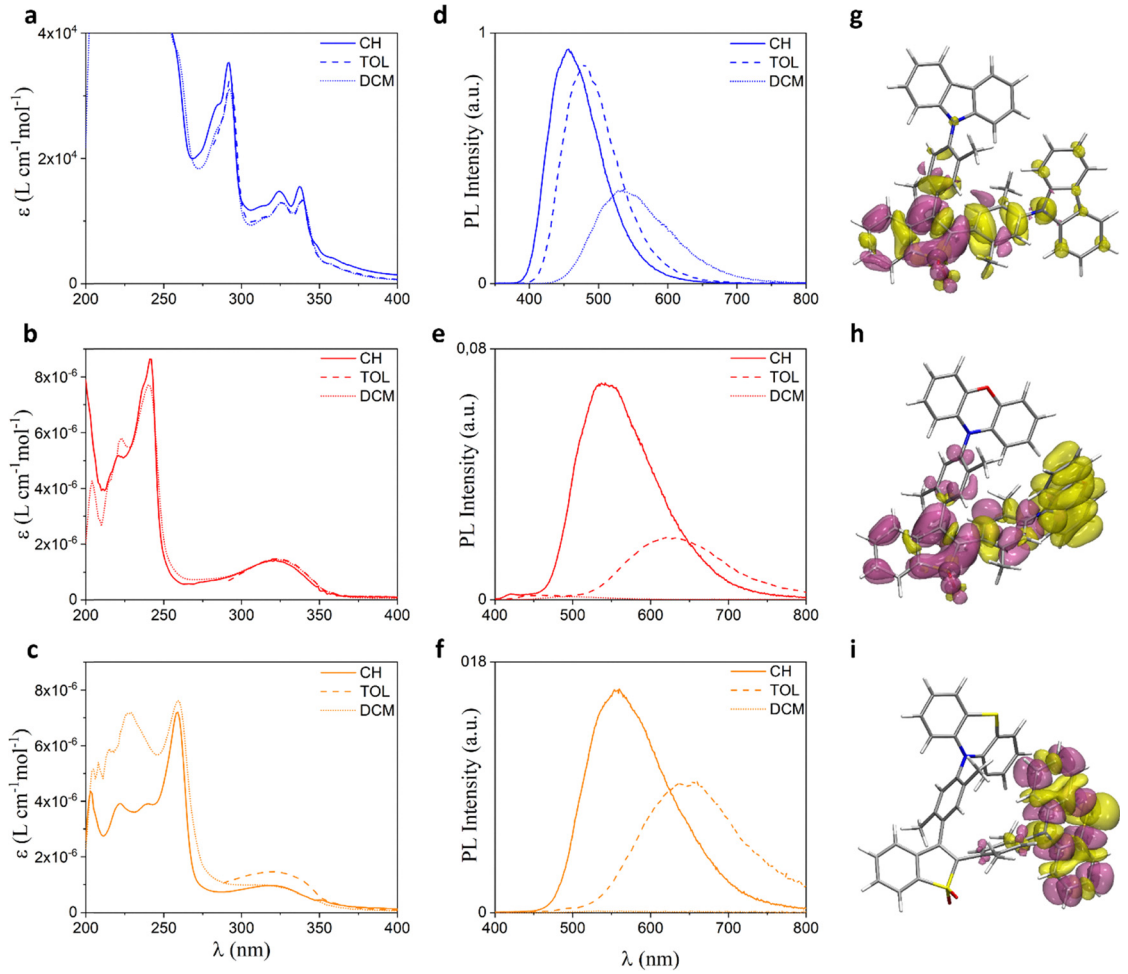

Fig. 1 UV-vis absorption (a–c) and PL spectra (d–f, normalized for their PLQY values) of **V-CBZ$_2$**, **V-POZ$_2$**, and **V-PTZ$_2$**, respectively, recorded in different solvents: CH (10^{-5} M, dotted line), TOL (10^{-5} M, dash-dotted line), and DCM (10^{-5} M, solid line). TD-DFT optimized geometries of the S_1 state (at the Franck–Condon region) for **V-CBZ$_2$** (g, 2.52 eV above the S_0), **V-POZ$_2$** (h, 2.62 eV above the S_0), and **V-PTZ$_2$** (i, 3.04 eV above the S_0), in DCM. Density differences ($\rho_{S_1}-\rho_{S_0}$) are used to describe the nature of each state: yellow (or pink) isosurfaces correspond to regions with a decrease (or increase) in the electron density with respect to the ground state (isovalue: 0.0005 e Bohr^{-3}).

spacers are able to keep the linked moieties in a nearly perpendicular arrangement, effectively minimizing the π-conjugation between the spacers and the D (or A) units; (iii) the distance between the centroids of the D and the A is about (9.7 ± 0.4) Å, regardless of the donor nature and the asymmetry of the two branches (see Table S3).

This spatial arrangement prevents effective π-conjugation and orbital overlap between the donor and acceptor moieties (as shown in the electrochemical section, see below), explaining the predominantly localized character of the electronic transitions and the minimal spectral changes compared to the individual D and A units. Furthermore, the negligible solvatochromism observed in the absorption spectra across the three investigated solvents (Fig. 1a–c) indicates that the brightest electronic transitions are only weakly influenced by medium polarity, further reinforcing that the engineered geometry of the molecular backbone leads to weak D–A coupling.

The experimental absorption spectra of all the investigated compounds have been correlated to the electronic vertical excitations computed by TD-DFT (Fig. S25). The lowest electronic transitions arise from a complex interplay between local-excited (LE) and charge-transfer (CT) excitations, the latter set involving both D and A units (Tables S4–S6). In **V-CBZ$_2$**, the lowest-energy singlet excitation (*i.e.*, $S_0 \rightarrow S_1$, estimated at 4.36 eV; see Table S4) is predominantly an LE excitation on the benzothiophene *S*,*S*-dioxide acceptor, with a non-negligible CT contribution from the **CBZ** donors (*i.e.*, hybrid LE/CT character; Fig. 1g). In contrast, **V-POZ$_2$** exhibits two virtually degenerate states (S_1 and S_2) at (3.88 ± 0.01) eV above the S_0 minimum, with CT character from **POZ** to the spacer/acceptor (Table S5 and Fig. 1h); notably, LE states centered on the two donors are estimated to lie 0.15 eV higher in energy. The situation is reversed in **V-PTZ$_2$**, where the two degenerate S_1 and S_2 states, found at 4.01 eV, are primarily LE excitations localized on the **PTZ** donors (Fig. 1i), and the CT states are 0.26 eV higher in energy (Table S6).

2.2.2. Emission properties. As shown in Fig. 1d–f, differently from what was observed in the absorption spectra, the

Table 1 Photophysical parameters of investigated compounds

	Cyclohexane						Toluene						Dichloromethane					
Compound	λ_{em} [nm]	PLQY [%]	t [ns]	k_r [10^7 s^{-1}]	k_{nr} [10^7 s^{-1}]	Φ_Δ [%]	λ_{em} [nm]	PLQY [%]	t [ns]	k_r [10^7 s^{-1}]	k_{nr} [10^7 s^{-1}]	Φ_Δ [%]	λ_{em} [nm]	PLQY [%]	t [ns]	k_r [10^7 s^{-1}]	k_{nr} [10^7 s^{-1}]	Φ_Δ [%]
V-CBZ$_2$	455	84.3	5.34	15.8	2.94	20	480	86.7	6.73	12.9	1.98	12	533	50.3	12.25	4.10	4.06	43
V-POZ$_2$	545	8.75	8.06	1.09	11.3	77	625	3.22	6.05	0.532	16.0	55	≈730	<0.1	—	—	—	—
V-PTZ$_2$	557	2.17	4.48	0.485	21.8	89	646	1.57	6.75	0.233	14.6	48	≈800	<0.05	—	—	—	—

photoluminescence (PL) spectra of **V-CBZ$_2$**, **V-POZ$_2$**, and **V-PTZ$_2$**: (i) are red-shifted compared to the emission spectra of individual donor and acceptor units (Fig. S24), and (ii) are strongly influenced by the polarity of the solvent, indicating that the emission originates from a different, more polar excited state. Furthermore, **V-POZ$_2$** and **V-PTZ$_2$** exhibit larger Stokes shifts than **V-CBZ$_2$** (see Table S2), particularly in CH and TOL, consistent with stronger intramolecular CT character and greater geometrical relaxation upon excitation.

In particular, upon increasing solvent polarity, **V-CBZ$_2$** displays a progressive red-shift in emission maximum (from 455 nm in CH to 480 nm in TOL and 533 nm in DCM; see Table 1), suggesting progressive stabilization of the hybrid LE-CT state. Both **V-POZ$_2$** and **V-PTZ$_2$** similarly show broad, unstructured fluorescence bands, which are markedly red-shifted when moving from CH to TOL (545 → 625 nm and 557 → 646 nm, respectively; see Table 1) and are strongly quenched in DCM, indicative of progressive stabilization and overstabilization of a potentially emissive CT state in both cases.

Interestingly, TD-DFT calculations revealed that in **V-PTZ$_2$**, the excited S_3 state – displaying strong CT character – can relax much more than S_1 or S_2, which are of LE nature, resulting to be lower in energy (0.13 eV) than the S_1 minimum (Fig. S26 and Table S6). This suggests that S_3 is likely responsible for the main fluorescence emission of **V-PTZ$_2$**. Notably, the sensitivity of **V-PTZ$_2$**'s emission to solvent polarity, which closely resembles that of **V-POZ$_2$**, further supports this assignment.

2.2.3. PL quantum yields (PLQY) and singlet oxygen generation. As summarized in Table 1, the PLQYs decrease markedly from **V-CBZ$_2$** to **V-POZ$_2$** and **V-PTZ$_2$**, reflecting the effect of increasing donor strength, which stabilizes CT states and enhances non-radiative decay, thus quenching the fluorescence.

Among the three compounds, **V-CBZ$_2$** consistently exhibits the highest PLQY, according to its relatively higher oscillator strength for the $S_1 \rightarrow S_0$ transition (f = 0.216 for **V-CBZ$_2$**, f = 0.030 for **V-POZ$_2$**, and f = 0.019 for **V-PTZ$_2$**). Additionally, increasing solvent polarity further reduces efficiency, especially for **V-POZ$_2$** and **V-PTZ$_2$**, consistent with the well-known stabilization of CT states in polar environments.[41]

In oxygen-free conditions, all compounds display higher PLQYs, indicating that molecular oxygen contributes to reducing the emission efficiencies in air-equilibrated solutions; therefore, triplet–triplet energy-transfer processes are expected to be important in the deactivation pathways of these compounds.[42]

To further elucidate the role of triplets and ISC processes, the efficiency of $^1O_2$ sensitization was evaluated from its phosphorescence at 1270 nm in air-equilibrated solutions (Fig. S27 and Table 1). Notably, unrestricted DFT calculations predict the presence of several low-lying triplet states located at approx. 2.15 eV above S_0 (Fig. S28), hence well above the threshold for energy transfer to ground-state molecular oxygen (≈0.98 eV). Moreover, TD-DFT calculations, carried out at the S_1 minimum-energy geometries, suggest potentially effective ISC pathways, owing to favorable SOC values and relatively small single-triplet energy differences (ΔE_{ST}), particularly for **V-POZ$_2$** and **V-PTZ$_2$** derivatives (Fig. S29).

In CH, both **V-POZ$_2$** and **V-PTZ$_2$** display low PLQYs due to very fast non-radiative decay rates (Table 1), which most likely arise from rapid ISC to non-emissive triplets, as indicated by their efficient $^1O_2$ generation (Φ_Δ = 77% and 89%). In contrast, **V-CBZ$_2$** exhibits a much higher PLQY and a large k_r, indicative of a predominantly fluorescent decay pathway, and a correspondingly lower $^1O_2$ yield ($\Phi_\Delta \approx$ 20%). In TOL, the modest increase in solvent polarity enhances the CT character and decreases both radiative and non-radiative decay rates for all compounds, resulting in a general reduction in PLQYs and Φ_Δ. Remarkably, in DCM, **V-POZ$_2$** and **V-PTZ$_2$** become virtually non-emissive due to the over-stabilization of their CT states, which promotes effective $S_1 \rightarrow S_0$ non-radiative relaxation, likely due to the energy-gap law,[43] consistent with the absence of $^1O_2$ sensitization. In contrast, **V-CBZ$_2$** shows a pronounced increase in Φ_Δ (≈ 43%), accompanied by a significant lifetime extension (τ = 12.3 ns) due to the reduction of k_r, suggesting an increase in the CT nature of its hybrid LE-CT state in such a polar solvent, which likely enhances singlet–triplet coupling, facilitating more efficient ISC and $^1O_2$ sensitization.

2.2. Electrochemical characterization

The redox properties of **V-CBZ$_2$**, **V-POZ$_2$**, and **V-PTZ$_2$** were investigated by cyclic voltammetry (CV). The corresponding voltammograms are shown in Fig. 2a, and the data are summarized in Table S7.

All compounds exhibit reversible reduction waves at essentially identical potentials ($E_{red} \sim -1.9$ eV), consistent with a fully reversible process localized on the common benzothiophene *S*,*S*-dioxide acceptor. This aligns with DFT calculations (Fig. S30), which show nearly identical LUMO energies across the series. Consistently, the computed spin density of the one-electron reduced radical anion is localized on the benzothiophene *S*,*S*-dioxide, corroborating that the reduction process is confined to the acceptor core. Spin-unrestricted DFT (*U*-DFT) further estimates a reduction potential of (−2.18 ± 0.03) V for all molecules (Fig. 2b), in agreement with experimental data (Table S7).

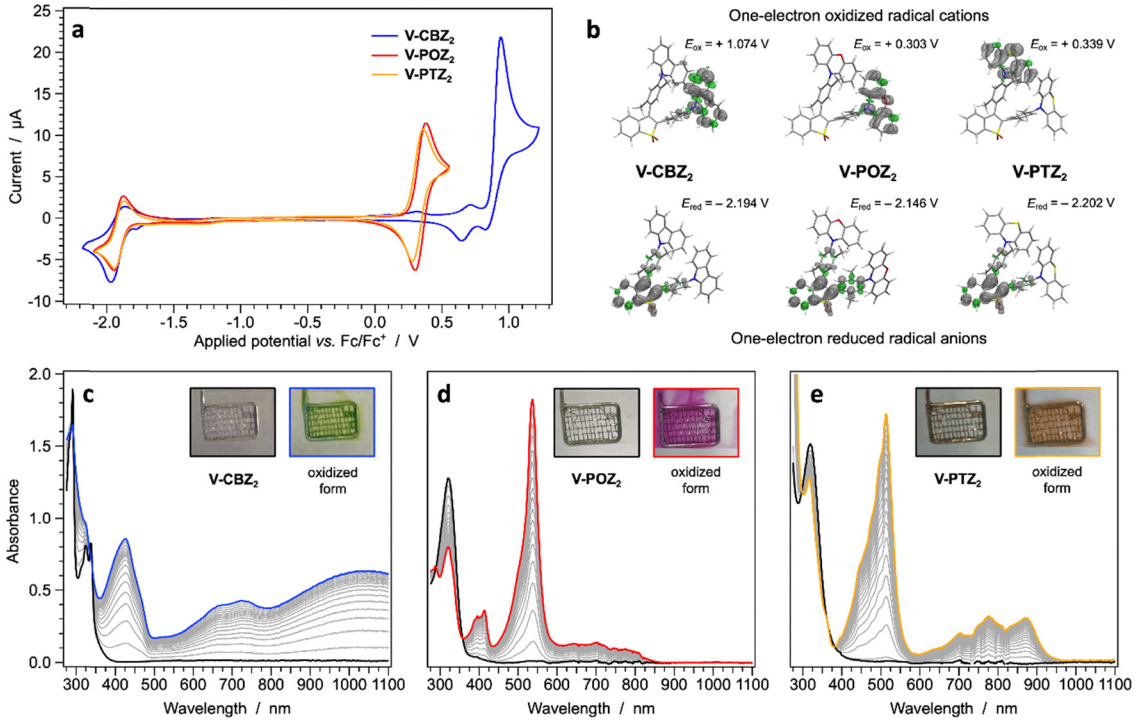

Fig. 2 Cyclic voltammograms of **V-CBZ$_2$**, **V-POZ$_2$**, and **V-PTZ$_2$** in acetonitrile solution at 298 K (sample concentration: 1.0 mM) (a). Spin-density distributions of the one-electron oxidized and reduced radicals of **V-CBZ$_2$**, **V-POZ$_2$**, and **V-PTZ$_2$** in their fully relaxed geometries, resulting from optimizations at the CAM-B3LYP-D4/def-SVP level of theory, computed by spin-unrestricted DFT in DCM (isovalue: 0.002 e Bohr^{-3}) (b); the DFT-estimated redox potentials *vs.* the ferrocene/ferrocenium couple are also reported. Spectral changes occurring upon oxidation of the investigated samples by applying a constant voltage of (E_{ox} + 0.1) V *vs.* Fc/Fc$^+$ (c–e); photographs of the compounds in their neutral (colourless) and oxidized (coloured) states are also reported.

On the contrary, the oxidation potential considerably changes along the series. The lowest oxidation potential is observed for **V-PTZ$_2$**, closely followed by **V-POZ$_2$** (*i.e.*, +0.32 *vs.* +0.34 V). While a much higher oxidation potential is found for **V-CBZ$_2$** (*i.e.*, +0.90 V), in agreement with the lower donating character of the CBZ unit compared to the POZ and PTZ.

Notably, the multiple oxidation features observed for **V-CBZ$_2$**, which persist even if using different working electrodes (Fig. S31), are tentatively attributed to intramolecular carbazole–carbazole interactions upon oxidation (*e.g.*, aggregation or electro-dimerization), likely due to the proximity of the two carbazole donors in such V-shaped D–π–A–π–D molecules.[44,45] Additionally, **V-CBZ$_2$** shows slight cycle-to-cycle differences, with minor peaks appearing prior to the main oxidation after the first cycle, indicative of secondary electrochemical processes (Fig. S32). In contrast, **V-POZ$_2$** and **V-PTZ$_2$** exhibit fully reversible behavior, as evidenced by the near-perfect overlap of successive CV scans.

In all cases, the oxidation process is bielectronic with respect to the one-electron reduction, as reflected by oxidation peak currents approximately twice those of the corresponding reductions. In line with this, DFT calculations indicate that all molecules present a HOMO and HOMO–1, which are very close in energy, centered on the two nearly equivalent donor units (Fig. S30). Thus, the energy of such orbitals clearly depends on the donor strength of the selected units, with the carbazole of **V-CBZ$_2$** leading to the most stabilized HOMO and HOMO−1 couple. Accordingly, the radical-cation spin density is likewise centered on the donor units, and *U*-DFT calculations estimate oxidation potentials nicely matching the observed experimental value (Fig. 2b). Notably, as shown in Fig. 2c–e, all three compounds are optically transparent in their neutral state, consistent with the absence of significant absorption in the visible region (Fig. 1a–c). Upon electrochemical oxidation, distinct absorption bands emerge in the visible and NIR range, consistent with the formation of radical cation species (oxidized forms). Within the series, **V-CBZ$_2$** exhibits more pronounced low-energy/broader polaronic features that extend well beyond 1100 nm, indicative of greater radical-cation delocalization compared to **V-POZ$_2$** and **V-PTZ$_2$**, likely attributable to its hybrid LE-CT character. This electrochromic switching leads to visible colour changes, with the specific colour dependent on the donor unit (see insets in Fig. 2c–e).

2.4. Steady-state and time-resolved PL emission in polymer matrices and neat films.

PL spectra of **V-CBZ$_2$**, **V-POZ$_2$**, and **V-PTZ$_2$** were evaluated in PMMA matrices (0.1 wt%) and in drop-casted neat films. In both environments, all compounds exhibit broad, featureless emission bands with lower PLQY compared to their solution phase counterparts (Fig. 3a and b and Table S8).

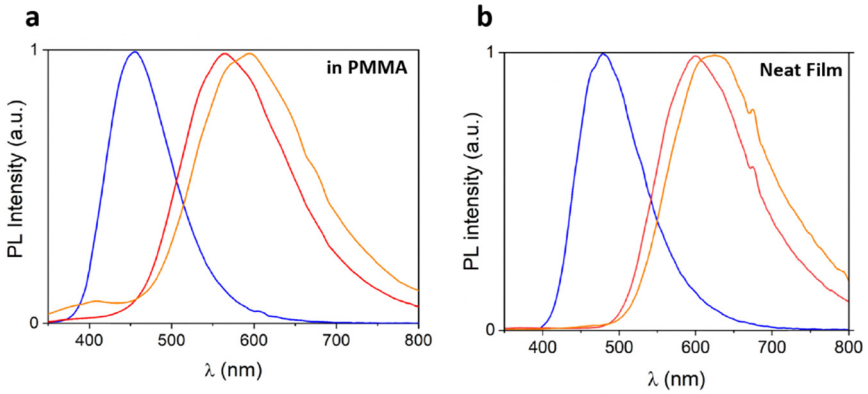

Fig. 3 Normalized steady-state PL spectra of **V-CBZ$_2$** (blue line), **V-POZ$_2$** (red line), and **V-PTZ$_2$** (orange line): (a) 0.1 wt% in PMMA and (b) neat film.

When moving from the rigid, dispersed environment of PMMA matrices to the more densely packed neat films, the PL spectra undergo a slight red shift (30–40 nm). Nevertheless, the PLQY remains comparable in both environments (Table S8),

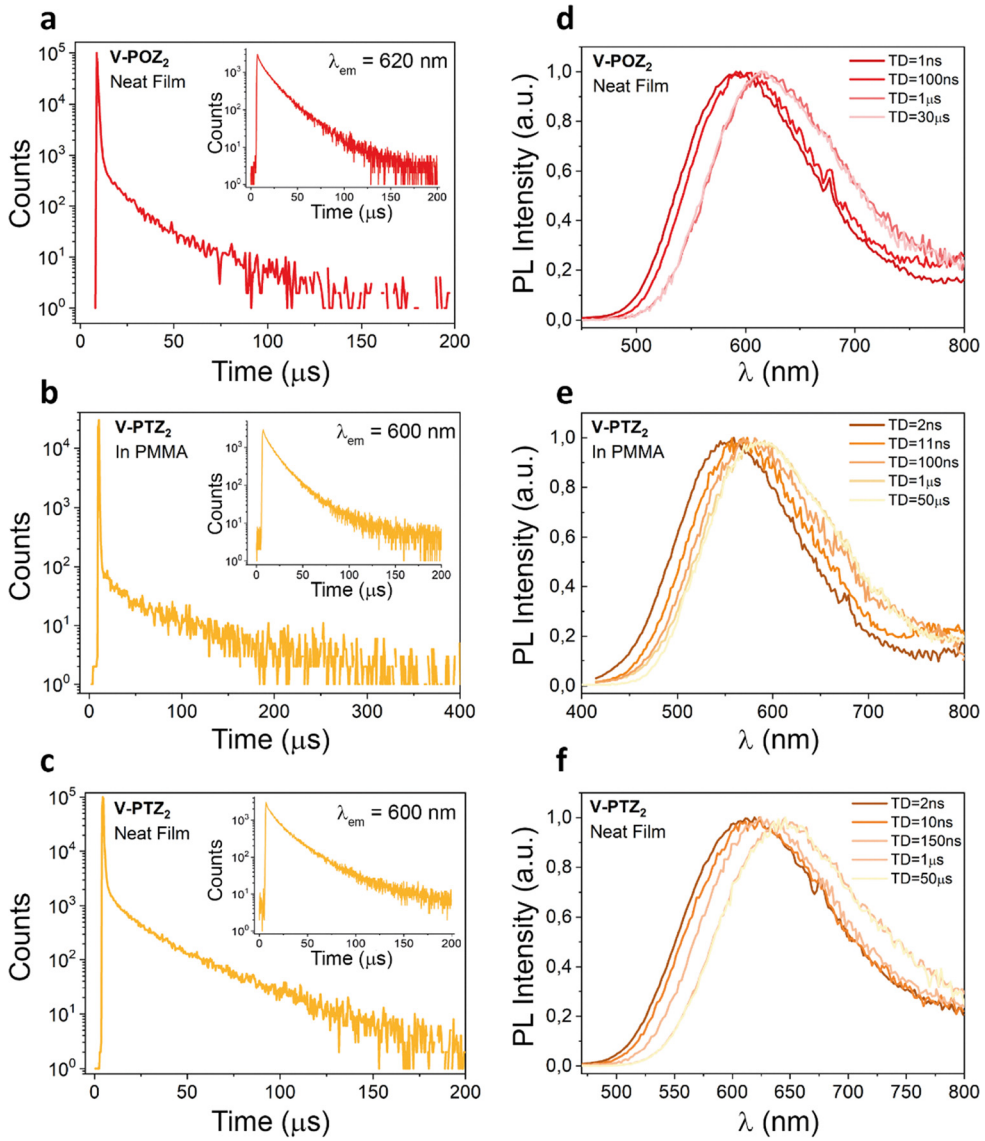

Fig. 4 Decay PL and time-resolved emission spectra of **V-POZ$_2$** as a neat film (a and d), and **V-PTZ$_2$** in PMMA (0.1 wt%) (b and e) and neat film (c and f).

supporting that the V-shaped geometry of the molecules in thin film effectively suppresses tight π–π stacking and thereby prevents AIQ. The observed red shift in the neat films is, therefore, more plausibly attributed to intermolecular stabilization of the excited state in the densely packed environment rather than to strong π–π interactions. This interpretation is supported by X-ray diffraction (XRD) analysis, which confirms the amorphous nature of all thin films (Fig. S33), indicating the absence of long-range crystalline order.

Time-resolved PL measurements (TRPL), performed at room temperature in both PMMA matrices and neat films under deoxygenated conditions, reveal distinct decay pathways across the series (see Table S8). **V-CBZ$_2$** exhibits exclusively prompt fluorescence (PF), with the decay fully resolved within the nanosecond regime in both environments (Fig. S34a and b). In contrast, **V-POZ$_2$** and **V-PTZ$_2$** display dual decay regimes characterized by a fast nanosecond (PF) and a slower microsecond component indicative of delayed fluorescence (DF). In particular, **V-POZ$_2$** shows only PF in PMMA, whereas an additional DF contribution emerges in neat films (Fig. 4a and Fig. S34c). Conversely, **V-PTZ$_2$** displays clear DF signatures in both media (Fig. 4b and c).

For the samples exhibiting DF, time-resolved emission spectroscopy (TRES) was also performed, allowing the reconstruction of individual spectra at specific time delays (see SI for details). As shown in Fig. 4d–f, in all cases the emission spectra remain similar over time, indicating that both PF and DF arise from the same singlet excited state. In particular, PF is slightly blue-shifted with respect to DF, a behaviour commonly reported for D–A systems and usually ascribed to slow geometrical relaxation and to a distribution of CT conformations, with the delayed component dominated by more relaxed, lower-energy CT states.[27,46,47] The observed delayed emission is generally attributed to TADF and, in some cases, possibly to triplet–triplet annihilation (TTA). However, the bi-excitonic TTA is extremely unlikely at 0.1 wt% in PMMA films, where the emitters are well-isolated.[48,49]

To further clarify the origin of the delayed component, time-gated delayed PL measurements were performed at 77 K in toluene (*i.e.*, under rigid, glassy conditions). Under these conditions, phosphorescence was detected only for **V-PTZ$_2$**, with spectral features matching those of the PTZ donor, indicative of a donor-localized triplet (^{3}LE$_D$) (Fig. S35). Notably, the absence of phosphorescence for **V-CBZ$_2$** and **V-POZ$_2$** is consistent with the absence of DF in PMMA matrices. The triplet state energy for **V-PTZ$_2$**, estimated from the phosphorescence onset, is E_T = 2.57 eV, whereas the singlet CT energy, obtained from the onset of the delayed emission (TD = 1 μs), is E_S = 2.62 eV. This results in a small ΔE_{ST} of 0.05 eV, confirming the TADF nature of the DF observed at room temperature for **V-PTZ$_2$**.

Regarding the decay profiles, the PF component (nanosecond domain) of all compounds was fitted using bi- or

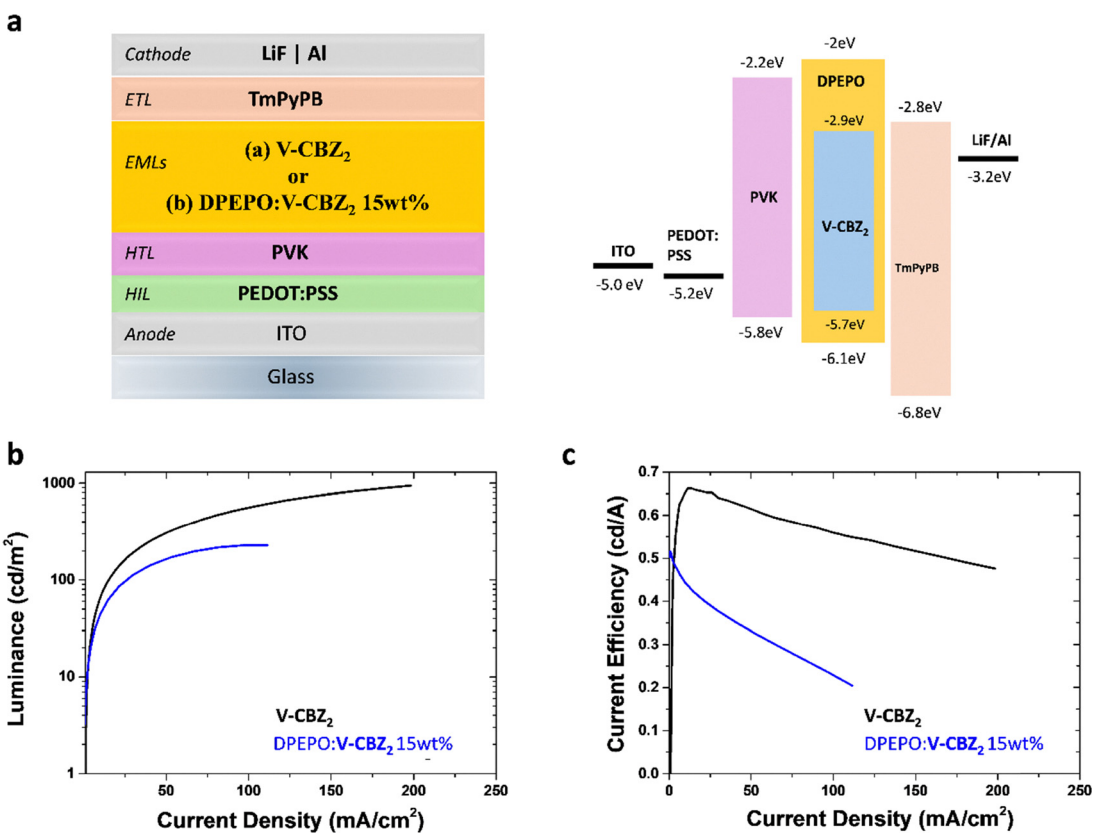

Fig. 5 (a) Structure of the multilayer electroluminescent devices (left) and energy levels of the materials used (right). (b) Luminance *vs.* current density and (c) current efficiency *vs.* current density curves of both neat and doped **V-CBZ$_2$**-based emissive films.

tri-exponential functions (Table S8). The two shortest lifetime components are assigned to PF emissions, likely originating from the ^{1}LE state of the donor and the ^{1}CT states, while the longer component may arise from weakly aggregated species or from the tail of the DF region. The DF component (microsecond domain) also follows a bi-exponential decay with characteristic average lifetimes (τ_{av}) reported in Table S8. For **V-PTZ$_2$** in PMMA, both DF decay components can be reliably attributed to TADF. In neat films of **V-POZ$_2$** and **V-PTZ$_2$**, however, we cannot exclude that the observed DF could arise from TADF involving aggregated species with possible contribution from TTA processes.[50]

2.5. Organic light-emitting diodes (OLEDs) fabrication

Owing to its favorable photophysical properties, **V-CBZ$_2$** was tested as an emissive material in bottom-emitting OLED devices, either as a neat film or dispersed in a concentration of 15% in bis[2-(diphenylphosphino) phenyl]ether oxide (DPEPO) host matrix (Fig. 5).

V-CBZ$_2$ proved to be an efficient electroluminescent (EL) material in both device configurations. As shown in Fig. S36a, the EL spectra of the **DPEPO:V-CBZ$_2$** blend mirror the photophysical behaviour observed in CH solution and remain essentially unchanged across the explored voltage range. This spectral invariance, together with the stable CIE coordinates (x = 0.212–0.214; y = 0.253–0.256, bias 13–16 V, indicative of blue emission), suggests efficient exciton confinement and energy transfer within the host–guest system.[51–53] By contrast, when employed as a pure film, **V-CBZ$_2$** exhibits a much broader EL spectrum than its PL, likely due to interfacial exciplex formation with the charge-transport interlayers (HTL/ETL).[54,55] Notably, the emission covers the entire visible range, yielding CIE coordinates (x = 0.327–0.331; y = 0.373–0.394) that fall within the white-light region (Fig. S36b).

Neat film devices yield superior performance, with luminance values approaching 1000 cd m^{-2} and current efficiency ranging from 0.65 to 0.5 cd A^{-1}. By contrast, **DPEPO:V-CBZ$_2$** devices attain only $\sim$200 cd m^{-2} with current efficiencies between 0.5 and 0.2 cd A^{-1}. Both devices reach a maximum EQE of approximately 0.3%, with the neat **V-CBZ$_2$**-based device showing a reduced efficiency roll-off compared to **DPEPO: V-CBZ$_2$** at higher current densities (turn-on voltages: 8.2 V and 11.4 V, respectively, see Fig. S37).

This behaviour is noteworthy, as in analogous systems based on V-shaped molecules containing benzothiophene *S*,*S*-dioxide previously reported,[30] neat films typically suffered from severe AIQ. By comparison, the newly engineered architectures appear to effectively mitigate detrimental intermolecular interactions, allowing emission even superior to that observed in the host matrix and validating the molecular design rationale for solution-processable OLED applications.

III. Conclusions

We have introduced and systematically investigated a series of twisted V-shaped D–π–A–π–D small molecules (**V-CBZ$_2$**, **V-POZ$_2$**, **V-PTZ$_2$**), characterized by a common rigid benzo[*b*]thiophene *S*,*S*-dioxide acceptor core and identical π-spacers covalently linked to donor moieties of different strength (CBZ < POZ ≈ PTZ). In all molecules, the non-planar V-shaped geometry electronically decouples donor and acceptor moieties.

CV and spectroelectrochemistry reveal reversible acceptor reduction and donor oxidation with marked visible-NIR absorption changes, evidencing electrochromic switching between essentially transparent and coloured states.

Steady-state and time-resolved spectroscopy, supported by TD-DFT calculations, show that the donor strength varies the nature of the emissive states which evolves from a hybrid LE–CT character in **V-CBZ$_2$** to predominantly CT in **V-POZ$_2$** and **V-PTZ$_2$**.

In solution, **V-CBZ$_2$** results to be a highly emissive fluorophore with moderate $^1O_2$ generation, whereas **V-POZ$_2$** and **V-PTZ$_2$** are poorly emissive but very efficient $^1O_2$ photosensitizers (Φ_Δ up to 89%). Notably, these high singlet oxygen yields demonstrate the strong potential of these compounds as effective organic photosensitizers for applications such as photodynamic therapy and photocatalysis.[56–59] Overall, increasing solvent polarity stabilizes the CT states and thereby reshapes the balance between fluorescence and triplet harvesting across the series.

In the solid state, all molecules generate amorphous films with negligible long-range order, indicating that the twisted V-shaped architectures effectively mitigate π–π stacking. The stronger electron-donating groups (POZ and PTZ) promote the appearance of microsecond delayed fluorescence components, assigned to TADF mechanism. In contrast, the weaker donor (CBZ) in **V-CBZ$_2$** ensures efficient prompt fluorescence. Remarkably, neat **V-CBZ$_2$** films integrated into prototype OLEDs deliver broad white electroluminescence and outperform their matrix-dispersed counterparts, validating the design strategy and underscoring the potential of these V-shaped architectures for matrix-free, solution-processable light-emitting materials.

IV. Experimental section

4.1. DFT calculations

All calculations have been performed with the ORCA 6.0.1 program system,[60] considering dichloromethane solvation effects through the conductor-like polarizable continuum model.[61] The CAM-B3LYP range-separated hybrid density functional was adopted for all DFT calculations,[62] and the D4 dispersion corrections were included to better consider possible π–π intermolecular interactions.[63] The def2-SVP was selected as the basis set for all atoms.[64] The resolution of identity approximation and the chain-of-spheres exchange method were always used to speed up DFT calculations.[65,66] All molecules were fully optimized, without any symmetry constraints, in both their ground state and, by using time-dependent DFT (TD-DFT), in the lowest singlet excited states. TD-DFT calculations were always carried out using the Tamm–Dancoff Approximation (TDA), even for simulating the electronic absorption spectra of the investigated compounds. To investigate

the nature of the singly reduced and singly oxidized radicals, geometry optimizations and frequency calculations were performed at the spin-unrestricted CAM-B3LYP-D4/def2-SVP level of theory (imposing a spin multiplicity of 2), using the S_0 minimum-energy geometry as initial guess; the related redox potentials were estimated considering the difference in the energy of the radicals and that of the ground state, compared to the one of the ferrocene/ferrocenium couple. All pictures were created using the VMD software (Visual Molecular Dynamics).[67]

4.2. Photophysics

UV-vis absorption measurements (scan mode) were collected using a Cary 300 double beam spectrophotometer using rectangular 10 mm path length quartz cuvettes from Hellma at 25 °C. The absorption spectra were collected with concentrations in the range 10–20 μM (total volume 10 mL volumetric flask). For all the solvents, dilutions were made from a stock solution in chloroform at 1 mg mL^{-1}. Fluorescence spectroscopic studies were performed with an Edinburgh FLS980 spectrometer equipped with a Peltier-cooled Hamamatsu R928 photomultiplier tube (PMT, spectral window: 185–850 nm) at 25 °C and a NIR-sensitive R5509-72 InP/InGaAs PMT (spectral window: 300–1700 nm) for the evaluation of singlet-oxygen phosphorescence spectra and related quantum yields. For the analysis in solid state, the materials were dispersed in a rigid polymer matrix (PMMA) or as neat films obtained by drop-casting toluene solutions and deposited on quartz substrates, yielding optically thick layer with typical thicknesses of tens of micrometers. Corrected spectra were obtained *via* a calibration curve supplied with the instrument. For the excitation and emission spectra, the slit widths were adjusted between 1–5 nm, integration time 0.1 s, 1 nm step. The relative photoluminescence quantum yields (PLQY, Φ_{PL}) in solution were determined at 25 °C, from corrected emission spectra using quinine sulfate in 0.1 M $HClO_4$ as the standard. For each QY measurement, slit width, excitation wavelength, scan rate, integration time, and emission range were kept identical for the reference and the sample. The fluorescence QY was determined thanks to the following formula:

$$\Phi_{PL} = \Phi_R \cdot \left(\frac{Abs_R}{Abs_S}\right) \cdot \left(\frac{\eta_S{}^2}{\eta_R{}^2}\right) \cdot \left(\frac{I_S}{I_R}\right)$$

where: Φ_{PL} = Fluorescence quantum yield, Abs = absorbance of the solution, η = refractive index of the solvent, I = integrated fluorescence intensity of the emitted light, and subscripts "R" and "S" refer to the reference and sample, respectively. For all solid films, PLQYs were calculated by corrected emission spectra obtained from an apparatus consisting of a barium sulfate coated integrating sphere (4 or 6 inches), a 450 W Xe lamp (λ_{exc} = tunable by a monochromator supplied with the instrument) as light sources, and a R928 photomultiplier tube as signal detectors, following the procedure described by De Mello *et al.*[68]

Time-resolved PL experiments were performed in solution using 10 mm path length quartz cuvettes and in the solid-state, on thin films deposited on a quartz substrate.

Decay transients in the ns–μs range were measured using a time-correlated single-photon counting (TCSPC) setup (Edinburgh FLS980 spectrometer) equipped with a laser diode as excitation sources (EPL 1 MHz, λ_{exc} = 407 nm) and a peltier-cooled Hamamatsu R928 photomultiplier tube as detector. Delayed fluorescence for μs–ms range was measured using single photon counting multichannel scaling (MCS) with a variable pulse length diode laser (VPL-375, 100 Hz, λ_{exc} = 375 nm) as the excitation source.

MCS is complementary to TCSPC and is the method of choice for measuring delayed fluorescence over extended time ranges. In MCS the detection window is split into discrete time intervals, and all photons that arrive within a specified time interval are subsequently counted, allowing efficient collection of long-lived decay profiles. This multiple stop mode detection enables higher detection count rates than in TCSPC, reducing the acquisition time for longer decays. The pulse width of the VPL laser can be tuned from 100 ns to 1000 μs, for our measurements, it was set to 100 ns, providing sufficient power to the sample without obscuring the delayed fluorescence.

Luminescence decay profiles were analyzed using the DAS6 Decay analysis Software provided by Edinburgh Instruments. The quality of the fit was estimated by visual inspection of the weighted residuals and χ^2 minimization.

The method to record the PF and DF spectra is the time-resolved emission scan (TRES). In TRES measurements, emission decays are recorded as a function of emission wavelength, producing a three-dimensional dataset that can be integrated over selected time (10–20 s) windows to reconstruct PF and DF spectra. The high intensity and repetition rate of the VPL-375 laser enable rapid data collection, with full TRES profiles typically acquired within 20–40 minutes. Data integration was performed using the Fluoracle software associated with the FLS980 spectrometer. All measurements were carried out under deoxygenated conditions at 295 K and, in some case, under nitrogen flow at 77 K. Experimental uncertainties were estimated as: ±8% for lifetime determinations, ±20% for photoluminescence quantum yields, and ±2 nm/±5 nm for absorption and emission maxima, respectively.

4.3. Electrochemical characterization

Voltammetric experiments were performed using a Metrohm AutoLab PGSTAT302N electrochemical workstation in combination with the NOVA 2.1.6 software package. All the measurements were carried out at room temperature in acetonitrile solutions with a sample concentration of approximately 1.0 mM and using 0.1 M tetrabutylammonium hexafluorophosphate (electrochemical grade, $TBAPF_6$) as the supporting electrolyte. Oxygen was removed from the solutions by bubbling nitrogen. All the experiments were carried out using a three-electrode setup (BioLogic VC-4 cell, volume range: 1–3 mL) using a glassy carbon working electrode (having an active surface disk of 1.6 mm in diameter), the $Ag/AgNO_3$ redox couple (0.01 M in acetonitrile, with 0.1 M $TBAClO_4$ supporting electrolyte) as the reference electrode, and a platinum wire as the counter electrode. At the end of each measurement, ferrocene was added as the internal reference. Cyclic voltammograms (CV) were

recorded at a scan rate of 100 mV s^{-1}. Spectroelectrochemical measurements were carried out using the above-mentioned electrochemical setup, but using a spectroelectrochemical cell kit (Metrohm PTGRID-TRANSCELL, 1-mm optical path) with a platinum gauze working electrode; spectra were acquired using a coupled deuterium-halogen lamp (Avantes AvaLight-DHc) and an Avantes Starline spectrometer (AvaSpec ULS2048CL-EVO-RS, detection range: 200–1100 nm), controlled by AvaSoft 8.14.

4.4. Device fabrication and characterization

Patterned indium–tin oxide-coated glasses were sonicated in acetone and in 2-propanol for 10 min sequentially, then treated with O_2 plasma for 5 min to make the surface hydrophilic. PEDOT: PSS was spin-coated at 4000 rpm for 45 s, to give a 40-nm-thick HIL and annealed at 140 °C for 10 min to remove the residual solvent. An ETL chloroform: chlorobenzene solution of a high molecular weight PVK was spin-coated at 7000 rpm for 50 s, to give a 10 nm-thick film and annealed at 110 °C for 10 min. Emissive layers from chloroform:toluene solutions of neat **V-CBZ$_2$** and DPEPO:**V-CBZ$_2$** (15 wt%) were spin-coated at 2000 rpm for 50 s, to give the optimized thicknesses of 35 nm, then annealed at 110 °C for 10 min. All these organic films were spin-coated and annealed in ambient conditions. TmPyPB (45 nm) was deposited as the electron transport layer in a high vacuum chamber ($<10^{-7}$ Torr), as well as LiF (0.8 nm), and Al (100 nm). Film thicknesses were measured by ellipsometry. The current–voltage–luminance characteristics were measured in ambient conditions with an NIST calibrated Optronics OL770 spectrometer, coupled through an optical fiber to an OL610 telescope unit for the luminance measurements, and a Keithley 2420 current–voltage source-meter. All the devices were previously encapsulated in a nitrogen atmosphere. The EQE values were derived from the measured current efficiency and EL spectra, assuming a Lambertian emission distribution.[69]

Conflicts of interest

There are no conflicts to declare.

Data availability

The key data supporting the findings of this study are provided within the article and its supplementary information (SI). Complete raw datasets are available from the corresponding author upon reasonable request. Supplementary information: synthesis and characterization; photophysical properties; DFT calculations; electrochemical characterization; thin-film studies. See DOI: https://doi.org/10.1039/d5tc04245c.

Acknowledgements

We thank Dr Massimo Gazzano for XRD measurements. M. Z. and F. D. M. acknowledge project LiveSens (Air Force Office of Scientific Research (AFOSR) Projects: FA8655-22-1-7014), and the PRIN project EMBRACE (IntErLocked supraMolecular assemBlies in solution: the access key to new donoR–Acceptor multi Component architEctures, CUP Number: B53D23015460006). A. M. and F. M. acknowledge Italian Ministry of Research (MUR) under the complementary actions to the NRRP (PNC0000007) "Fit4MedRob-Fit for Medical Robotics" Grant (contract number CUP B53C22006960001).

References

1 A. Moliton, *Optoelectronics of molecules and polymers*, 2006, Springer.
2 A. Y. Takeda, *Acc. Chem. Res.*, 2024, **57**, 2219–2232.
3 S. J. Zou, Y. Shen, F. M. Xie, J. D. Chen, Y.-Q. Li and J. X. Tang, *Mater. Chem. Front.*, 2020, **4**, 788–820.
4 M. Zangoli, F. Monti, A. Zanelli, M. Marinelli, S. Flammini, N. Spallacci, A. Zakrzewska, M. Lanzi, E. Salatelli, F. Pierini and F. Di Maria, *Chem. – Eur. J.*, 2024, **30**, e202303590.
5 L. Wang and W. Zu, *Adv. Sci.*, 2024, **11**, 2307227.
6 X. Wan, C. Li, M. Zhang and Y. Chen, *Chem. Soc. Rev.*, 2020, **49**, 2828–2842.
7 M. Marinelli, A. Candini, F. Monti, A. Boschi, M. Zangoli, E. Salatelli, F. Pierini, M. Lanzi, A. Zanelli, M. Gazzano and F. Di Maria, *J. Mater. Chem. C*, 2021, **9**, 11216–11228.
8 M. Li, Dr. L. Hua, J. Zhao, Y. Liu, S. Yan and Z. Ren, *Angew. Chem., Int. Ed.*, 2025, **64**, e202501179.
9 X. Chen, X. Zhang, X. Xiao, Z. Wang and J. Zhao, *Angew. Chem., Int. Ed.*, 2023, **62**, e202216010.
10 F. Di Maria, M. Biasiucci, F. P. Di Nicola, E. Fabiano, A. Zanelli, M. Gazzano, E. Salatelli, M. Lanzi, F. Della Sala, G. Gigli and G. Barbarella, *J. Phys. Chem. C*, 2015, **119**, 27200–27211.
11 A. Maggiore, Y. Qu, R. Guillot, P. Pander, M. Vasylieva, P. Data, F. B. Dias, P. Audebert, G. Clavier and F. Miomandre, *J. Phys. Chem. B*, 2022, **126**, 2740–2753.
12 D. Conelli, A. Maggiore, R. Grisorio, G. P. Suranna, V. Maiorano, A. L. Sobolewski, W. Domcke, F. Miomandre and P. Audebert, *J. Phys. Chem. C*, 2025, **129**, 17249–17262.
13 O. P. Dimitriev, Dynamics of Excitons in Conjugated Molecules and Organic Semiconductor Systems, *Chem. Rev.*, 2022, **122**, 8487–8593.
14 R. Misra and S. P. Bhattacharyya, *Intramolecular Charge Transfer: Theory and Applications*, 2018, Wiley-VCH Verlag GmbH & Co. KGaA.
15 H. Shen, Y. Li and Y. Li, *Aggregate*, 2020, **1**, 57–68.
16 A. Maggiore, Y. Qu, P. Pander, F. B. Dias, G. Clavier, R. Guillot, D. Altamura, C. Giannini, V. Maiorano, P. Audebert and F. Miomandre, *J. Mater. Chem. C*, 2024, **12**, 7943–7955.
17 A. Maggiore, X. Tan, A. Brosseau, A. Danos, F. Miomandre, A. P. Monkman, P. Audebert and G. Clavier, *Phys. Chem. Chem. Phys.*, 2022, **24**, 17770–17781.
18 D. Puchán Sánchez, P. Josse, N. Plassias, G. Park, Y. Khan, Y. Park, M. Seinfeld, A. Guyard, M. Allain, F. Gohier, L. Khrouz, D. Lungerich, H. S. Ahn, B. Walker, C. Monnereau, C. Cabanetos and T. Le Bahers, *Chem. – Eur. J.*, 2024, **14**, e202400191.

19 Y. Zhou, L. Ma, A. V. Lunchev, S. Long, T. Wu, W. Ni, A. C. Grimsdale, L. Sun and G. G. Gurzadyan, *J. Phys. Chem. B*, 2021, **125**, 12518–12527.
20 K. Youssef, A. Gasonoo, M. Allain, H. Melville, L. Sanguinet, G. C. Welch and F. Gohier, *ACS Appl. Opt. Mater.*, 2024, **2**, 1610–1618.
21 K. Youssef, A. Gasonoo, C. Cougnon, M. Loumaigne, H. Melville, L. Sanguinet, G. C. Welch and F. Gohier, *Dyes Pigm.*, 2025, **232**, 112468.
22 D.-R. Bai, X.-Y. Liu and S. Wang, *Chem. – Eur. J.*, 2007, **13**, 5713–5723.
23 G. Barbarella, L. Favaretto, A. Zanelli, G. Gigli, M. Mazzeo, M. Anni and A. Bongini, *Adv. Funct. Mater.*, 2005, **15**, 4.
24 M. Melucci, L. Favaretto, G. Barbarella, A. Zanelli, N. Camaioni, M. Mazzeo and G. Gigli, *Tetrahedron*, 2007, **63**, 11386–11390.
25 B. Sk, S. Khodia and A. Patra, *Chem. Commun.*, 2018, **54**, 1786–1789.
26 A. M. Napper, N. J. Head, A. M. Oliver, M. J. Shephard, M. N. Paddon-Row, I. Read and D. H. Waldeck, *J. Am. Chem. Soc.*, 2002, **124**, 10171–10181.
27 M. Montrone, A. Maggiore, A. Moliterni, P. Pander, M. Pugliese, A. Lina Capodilupo, S. Gambino, C. T. Prontera, V. Valenzano, F. Mariano, G. Accorsi, T. Sibillano, C. Giannini, G. Gigli, A. Cardone and V. Maiorano, *J. Mater. Chem. C*, 2025, **13**, 160–176.
28 S. Sasaki, G. P. C. Drummen and G. Konishi, *J. Mater. Chem. C*, 2016, **4**, 2731–2743.
29 S. Ahmad, J. Eng and T. J. Penfold, *J. Phys. Chem. A*, 2024, **128**, 8035–8044.
30 F. Di Maria, M. Zangoli, I. E. Palamá, E. Fabiano, A. Zanelli, M. Monari, A. Perinot, M. Caironi, V. Maiorano, A. Maggiore, M. Pugliese, E. Salatelli, G. Gigli, I. Viola and G. Barbarella, *Adv. Funct. Mater.*, 2016, **26**, 6970–6984.
31 R. S. Nobuyasu, J. S. Ward, J. Gibson, B. A. Laidlaw, Z. Ren, P. Data, A. S. Batsanov, T. J. Penfold, M. R. Bryce and F. B. Dias, *J. Mater. Chem. C*, 2019, **7**, 6672–6684.
32 D. W. Lee, J. Hwang, H. J. Kim, H. Lee, J. M. Ha, H. Y. Woo, S. Park, M. J. Cho and D. H. Choi, *ACS Appl. Mater. Interfaces*, 2021, **13**, 49076–49084.
33 J. Marques dos Santos, D. Hall, B. Basumatary, M. Bryden, D. Chen, P. Choudhary, T. Comerford, E. Crovini, A. Danos, J. De, S. Diesing, M. Fatahi, M. Griffin, A. K. Gupta, H. Hafeez, L. Hämmerling, E. Hanover, J. Haug, T. Heil, D. Karthik, S. Kumar, O. Lee, H. Li, F. Lucas, C. F. R. Mackenzie, A. Mariko, T. Matulaitis, F. Millward, Y. Olivier, Q. Qi, I. D. W. Samuel, N. Sharma, C. Si, L. Spierling, P. Sudhakar, D. Sun, E. Tankelevičiūtė, M. D. Tonet, J. Wang, T. Wang, S. Wu, Y. Xu, L. Zhang and E. Zysman-Colman, *Chem. Rev.*, 2024, **124**, 13736–14110.
34 H. Takahashi, M. Kohri and K. Kishikawa, *Cryst. Growth Des.*, 2025, **25**, 4655–4660.
35 S. Bhuin, P. Chakraborty, P. Sivasakthi, P. K. Samanta, P. Yogeeswari and M. Chakravarty, *J. Mater. Chem. C*, 2023, **11**, 11270–11282.
36 M. Dutta, A. Chatterjee, N. Deka, R. Tanwar, V. Mishra, A. Saha, P. Mandal, R. Boomishankar and P. Hazra, *Chem. Sci.*, 2025, **16**, 11989–11998.
37 W. Che, Y. Xie and Z. Li, *Asian J. Org. Chem.*, 2020, **9**, 1262–1276.
38 P. Ruiz-Castillo and S. L. Buchwald, *Chem. Rev.*, 2016, **116**, 12564–12649.
39 N. F. F. Nathel, J. Kim, L. Hie, X. Jiang and N. K. Garg, *ACS Catal.*, 2014, **4**, 3289–3293.
40 T. Ishiyama, M. Murata and N. Miyaura, *J. Org. Chem.*, 1995, **60**, 7508–7510.
41 H. Song, K. Wang, Z. Kuang, Y. S. Zhao, Q. Guo and A. Xia, *Phys. Chem. Chem. Phys.*, 2019, **21**, 3894–3902.
42 F. M. Cabrerizo, J. Arnbjerg, M. P. Denofrio, R. Errabalsells and P. R. Ogilby, *ChemPhysChem*, 2010, **11**, 796–798.
43 R. Englman and J. Jortner, *Mol. Phys.*, 1969, **18**, 145–164.
44 J. F. Ambrose and R. F. Nelson, *J. Electrochem. Soc.*, 1968, **115**, 1159–1163.
45 M. Ates and N. Uludag, *J. Solid State Electrochem.*, 2016, **20**, 2599–2612.
46 Y. Takeda, *Acc. Chem. Res.*, 2024, **57**, 2219–2232.
47 A. Maggiore, Y. Qu, G. Clavier, M. Colella, A. Danos, A. Monkman, R. Guillot, M. Pugliese, C. T. Prontera, R. Giannuzzi, F. Mariano, S. Carallo, G. Accorsi, V. Maiorano, P. Audebert, R. Metivier and F. Miomandre, *J. Mater. Chem. C*, 2025, **13**, 13752–13767.
48 J. A. O'Brien, S. Rallabandi, U. Tripathy, M. F. Paige and R. P. Steer, *Chem. Phys. Lett.*, 2009, **475**, 220–222.
49 S. Mattiello, A. Danos, K. Stavrou, A. Ronchi, R. Baranovski, D. Florenzano, F. Meinardi, L. Beverina, A. Monkman and A. Monguzzi, *Adv. Opt. Mater.*, 2024, **12**, 2401597.
50 S. Debnath, P. Ramkissoon, U. Salzner, C. R. Hall, N. A. Panjwani, W. Kim, T. A. Smith and S. Patil, *Nat. Commun.*, 2025, **16**, 2982.
51 H. Nakanotani, T. Higuchi, T. Furukawa, K. Masui, K. Morimoto, M. Numata, H. Tanaka, Y. Sagara, T. Yasuda and C. Adachi, *Nat. Commun.*, 2014, **5**, 4016.
52 L. S. Cui, S. B. Ruan, F. Bencheikh, R. Nagata, L. Zhang, K. Inada, H. Nakanotani, L. S. Liao and C. Adachi, *Nat. Commun.*, 2017, **8**, 2250.
53 S. Reineke, K. Walzer and K. Leo, *Phys. Rev. B: Condens. Matter Mater. Phys.*, 2007, **75**, 125328.
54 S. P. Singh, Y. N. Mohapatra, M. Qureshi and S. S. Manoharan, *Appl. Phys. Lett.*, 2005, **86**, 113505.
55 M. Sarma, L. M. Chen, Y.-S. Chen and K.-T. Wong, *Mater. Sci. Eng. R Rep.*, 2022, **150**, 100689.
56 T. Zhang, X. Qu, J. Shao and X. Dong, *Chem. Soc. Rev.*, 2025, **54**, 8406–8433.
57 M. Zangoli and F. Di Maria, *View*, 2021, **2**, 20200086.
58 S. Flammini, M. Di Sante, P. E. Costantini, E. J. Mattioli, A. Marconi, E. Turrini, S. La Rosa, M. Montrone, T. D. Marforio, M. Nigro, N. Spallacci, A. Zanelli, M. Zangoli, A. Danielli, M. Di Giosia, F. Di Maria and M. Calvaresi, *J. Mater. Chem. B*, 2025, **13**, 12536–12546.
59 A. Cantelli, M. Malferrari, A. Solda, G. Simonetti, S. Forni, E. Toscanella, E. J. Mattioli, F. Zerbetto,

A. Zanelli, M. Di Giosia, M. Zangoli, G. Barbarella, S. Rapino, F. Di Maria and M. Calvaresi, *JACS Au*, 2021, **1**, 925–935.
60 F. Neese, *Comput. Mol. Sci.*, 2022, **12**, e1606.
61 M. Garcia-Ratés and F. Neese, *J. Comput. Chem.*, 2020, **41**, 922–939.
62 T. Yanai, D. P. Tew and N. C. Handy, *Chem. Phys. Lett.*, 2004, **393**, 51–57.
63 L. Wittmann, I. Gordiy, M. Friede, B. Helmich-Paris, S. Grimme, A. Hansen and M. Bursch, *Phys. Chem. Chem. Phys.*, 2024, **26**, 21379–21394.
64 F. Weigend and R. Ahlrichs, *Phys. Chem. Chem. Phys.*, 2005, **7**, 3297–3305.
65 F. Neese, *J. Comput. Chem.*, 2003, **24**, 1740–1747.
66 F. Neese, F. Wennmohs, A. Hansen and U. Becker, *Chem. Phys.*, 2009, **356**, 98–109.
67 W. Humphrey, A. Dalke and K. Schulten, *J. Mol. Graph.*, 1996, **14**, 33–38.
68 J. C. de Mello, H. F. Wittmann and R. H. Friend, *Adv. Mater.*, 1997, **9**, 230–232.
69 S. R. Forrest, D. D. C. Bradley and M. E. Thompson, *Adv. Mater.*, 2003, **15**, 1043–1048.

